Chemical Science

ROYAL SOCIETY OF CHEMISTRY

EDGE ARTICLE

View Article Online
View Journal | View Issue

Cite this: *Chem. Sci.*, 2026, **17**, 4753

All publication charges for this article have been paid for by the Royal Society of Chemistry

Active selenium-driven confined crystallization and carrier dynamics in high-efficiency ultrathin semi-transparent Sb_2Se_3 solar cells

Huafei Guo, *[ac] Bangzhi Shen,[a] Xing Wang,[d] Jiayu Xiao,[a] Wenyun Deng,[a] Sai Jiang,*[a] Lei Xu,[d] Xu Dong,*[c] Lvzhou Li,[c] Shuai Zhang, [b] Jianhua Qiu,*[a] Ningyi Yuan[b] and Jianning Ding[c]

To overcome the limited environmental stability of organic semi-transparent photovoltaic (STPV) devices, developing robust inorganic thin-film absorbers has become a critical research focus. Antimony selenide (Sb_2Se_3), with its Q1D crystal structure, excellent optoelectronic properties, and mechanical flexibility, is a promising candidate for STPV applications. However, thinning the absorber to enhance visible transmittance often degrades crystallinity, weakens preferred orientation, and increases defect density. Here, we present a dual-pathway device-engineering strategy that integrates KOH-assisted chemical-bath thinning of the CdS buffer layer with rapid thermal evaporation combined with magnetron sputtering of active selenium (Se). The introduced active Se atoms effectively reorganize molecular chains within a confined crystallization space, enhancing crystalline quality and promoting vertical [*hk*1] orientation. Simultaneously, Se doping passivates selenium vacancies and suppresses deep-level trap states, thereby improving carrier transport and reducing nonradiative recombination. Employing this strategy, we demonstrate for the first time an ultrathin Sb_2Se_3 STPV device with a total functional layer thickness of only 80 nm just one-seventh the thickness of conventional devices—achieving an efficiency of 7.02%, retaining 93% of that of thicker counterparts while maintaining an optical transparency exceeding 20%. This work establishes a practical route to simultaneously balance transparency and efficiency in inorganic STPV devices and underscores the potential of Sb_2Se_3 as a high-performance absorber for next-generation semi-transparent and tandem photovoltaics.

Received 24th October 2025
Accepted 8th January 2026

DOI: 10.1039/d5sc08223d

rsc.li/chemical-science

Introduction

In recent years, semi-transparent thin-film solar cells have garnered considerable attention due to their potential applications in building-integrated photovoltaics (BIPV), green lighting, and Internet of Things (IoT) sensors.[1–3] Although organic semi-transparent photovoltaic devices offer excellent tunability and can be constructed using a wide range of materials, they are typically hindered by poor environmental stability, short operational lifetimes, and susceptibility to thermal- and photodegradation.[4,5] These challenges impede their practicality for long-term deployment. Consequently, the development of inorganic semi-transparent thin-film solar cells with superior stability and controllable processing parameters is of significant scientific interest. Most inorganic semi-transparent photovoltaic devices currently rely on the use of three-dimensional semiconductor materials for their absorber layers, such as amorphous silicon (a-Si), copper indium gallium selenide (CIGS), and metal halide perovskites ($CsPbI_2Br$).[6–8] However, when these materials are thinned to achieve semi-transparency, they often exhibit deteriorated crystallinity, increased surface defects, and interfacial instability, which compromise carrier transport and overall efficiency.[9,10]

Antimony selenide (Sb_2Se_3), with its unique one-dimensional (1D) ribbon-like crystal structure, offers inherent structural advantages for the fabrication of ultrathin semi-transparent devices. It also exhibits a moderate bandgap (~1.2 eV), a high absorption coefficient, and a theoretical power conversion efficiency (PCE) exceeding 26%.[11,12] These properties enable good light absorption even at reduced thicknesses, positioning Sb_2Se_3 as a promising candidate for fabricating high-performance inorganic semi-transparent solar cells. However, the development of Sb_2Se_3-based devices presents several challenges. During the process of thickness reduction, the limited crystallization space can result in degraded crystal

[a]*Wang Zheng School of Microelectronics, Changzhou University, Changzhou 213164, China. E-mail: guohuafei@cczu.edu.cn; jhqiu@cczu.edu.cn*

[b]*School of Materials Science and Engineering, Changzhou University, Changzhou 213164, China*

[c]*Institute of Technology for Carbon Neutralization, School of Physical Science and Technology, Yangzhou University, Yangzhou 225127, China*

[d]*School of Flexible Electronics (Future Technologies), Institute of Advanced Materials (IAM), Nanjing Tech University, Nanjing 211816, China*

orientation, reduced grain size, and increased surface roughness. These structural deteriorations result in a higher density of deep-level defects, which, in turn, exacerbate carrier recombination and constrain optoelectronic performance.[13–15] Thus, maintaining high crystallinity and low defect density at the required absorber thickness remains a critical challenge in the development of efficient ultrathin semi-transparent Sb_2Se_3 devices.

Traditional solution-based fabrication methods such as chemical bath deposition (CBD) promote oriented crystal growth and suppress defect formation through controlled reaction kinetics.[16] However, CBD suffers from limited process flexibility, poor control over deposition conditions and film thickness, and insufficient uniformity. These issues are particularly problematic in the fabrication of nanometer-scale functional layers. Among various vacuum-based physical vapor deposition (PVD) techniques, magnetron sputtering is a commonly employed method for depositing Sb_2Se_3 films and has been widely used in the development of high-performance Sb_2Se_3 devices. However, these high-efficiency devices generally rely on high-temperature post-selenization to improve the crystallinity and stoichiometry of the films. Notably, the high-temperature selenization process can disrupt the device stack in superstrate architectures and significantly increase the sheet resistance of the FTO front electrode, thereby limiting its applicability in ultrathin transparent device structures.[17–21]

Comparatively, rapid thermal evaporation (RTE)—offers several comparative advantages, including precise control over film thickness, high deposition rates, stable processing, and excellent film uniformity.[22,23] These characteristics make RTE an attractive method for fabricating ultrathin photovoltaic structures. However, the fast deposition rates and limited atomic mobility inherent in RTE can lead to insufficient crystallization and degraded preferential orientation. Selenium (Se) is also prone to re-evaporation under high-temperature vacuum conditions, which results in selenium vacancy defects (V_{Se}) and antimony-on-selenium antisite defects (Sb_{Se}). These deep-level defects exacerbate carrier recombination and distort the local band structure, thereby impairing charge transport and collection.[24,25] Consequently, RTE alone is insufficient for ensuring both high crystallinity and low defect density in ultrathin Sb_2Se_3 absorber layers.

To address the limitations of conventional high-temperature selenization in ultrathin semi-transparent architectures, this study introduces a post-deposition Se compensation strategy utilizing magnetron sputtering for compositional and structural refinement.[26,27] High-energy active Se species not only compensate for the stoichiometric deviation caused by Se volatilization during the RTE process, but also fill vacancies and microvoids at the film surface and in the vicinity of grain boundaries and bond with unsaturated sites to achieve effective passivation, thereby suppressing the formation and activity of anion-vacancy-related deep-level defects such as V_{Se} and Sb_{Se} and mitigating their detrimental impact as nonradiative recombination centers on carrier transport and lifetime.[24,28,29] These active Se atoms also promote recrystallization and vertical preferential orientation, thereby enhancing crystal ordering and alignment. This compensation strategy significantly optimizes film quality, charge carrier migration pathways, and carrier lifetimes, thus enabling the effective regulation of carrier dynamics within the device. Using this optimization approach, we successfully fabricated an ultrathin Sb_2Se_3 semi-transparent solar cell with a total functional layer thickness of just 80 nm. The device demonstrated excellent photovoltaic performance and structural controllability with a PCE of 7.02% while maintaining visible light transmittance, which surpasses the performance of previously reported semi-transparent thin-film solar cells.[30–32] This work represents a promising direction for the development of stable, low-cost inorganic semi-transparent photovoltaic devices.

Results and discussion

In the structural design of semi-transparent Sb_2Se_3 thin-film solar cells, their optical and electrical performances are critically dependent both on the precise engineering of the absorber layer and on optimizing the thickness of the CdS buffer layer. Recent research on semi-transparent devices has predominantly focused on thinning the absorber layer to enhance overall light transmittance. This reduction in the thickness of the Sb_2Se_3 layer inherently shifts the heterojunction interface closer to the front contact, which alters the spatial distribution of the depletion region.[33] This shift necessitates an optimized CdS layer thickness to maintain appropriate band alignment and ensure that an optimal built-in electric field is maintained across the heterojunction, which is crucial for efficient charge separation and transport. Reducing the thickness of the CdS film can theoretically improve the absorption of the short-wavelength region, leading to increased current density.[34] However, excessive thinning of the CdS layer can deteriorate film crystallinity or increase interfacial defect density, thereby impairing carrier separation and charge-transport dynamics and even promoting sulfur diffusion from CdS into the Sb_2Se_3 absorber, which further accelerates device degradation.[35,36] Thus, achieving an optimal balance between minimizing crystallinity losses (through CdS thinning) and preserving the structural integrity and electronic performance of the heterojunction interface remains a significant challenge in the development of high-efficiency semi-transparent photovoltaic devices.[37,38] This balance is critical for maintaining high transmittance in the visible spectrum and efficient carrier dynamics, both of which are essential for improving overall device performance.

In this study, we developed a CBD strategy incorporating KOH as a dopant to achieve effective control over the crystallinity and optoelectronic performance during the process of thinning the CdS film. The schematic diagram and visual comparison of actual samples are presented in Fig. 1a and S1, and the detailed chemical bath deposition process is illustrated in Fig. S2. As shown in Fig. S3 and S4, this work presents the *J–V* characteristic curves and box plots of devices fabricated with different KOH concentrations in the CdS chemical bath, along with the corresponding schematic diagrams of the device structures. Based on these initial device results, we hypothesize

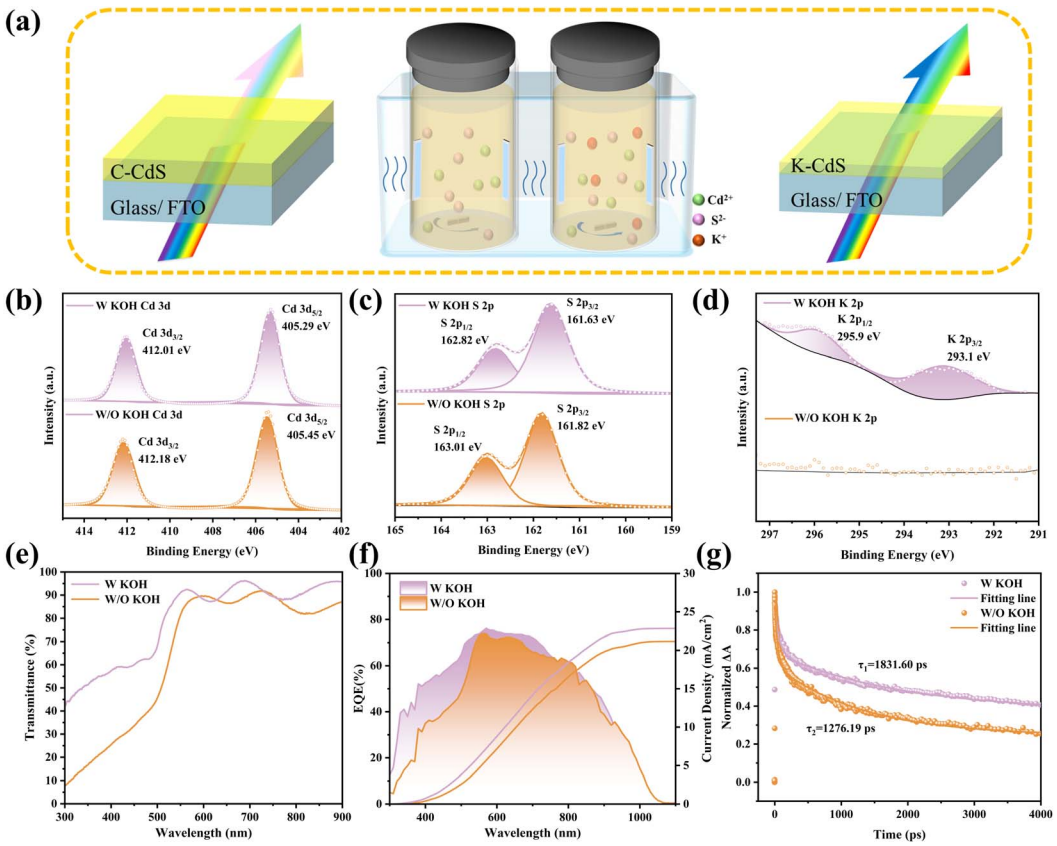

Fig. 1 (a) Schematic illustration of the CdS thin film deposition *via* chemical bath method, highlighting the structural differences between undoped (C-CdS) and K^+-doped (K-CdS) samples, along with their respective short-wavelength light transmittance characteristics. (b–d) XPS spectra of Cd 3d, S 2p, and K 2p. (e) the transmission spectra, (f) EQE plot, (g) carrier decay curves extracted from TAS.

that conventional CdS films (C-CdS) exhibit significant absorption in the ultraviolet-visible (UV-vis) spectral region, which limits the transmission of short-wavelength photons. Furthermore, when 5 mmol of K^+ ions are introduced into the precursor solution, these ions participate in the nucleation and grain–growth processes, giving rise to K^+-doped CdS films (K-CdS) with reduced thickness, improved crystallinity, and enhanced short-wavelength transmittance.

To further verify our hypothesis, we conducted detailed characterizations of the structure, morphology, and optoelectronic properties of both C-CdS and K-CdS films. The X-ray diffraction (XRD) patterns (Fig. S5) reveal that both films retained their characteristic hexagonal wurtzite phase (PDF # 41-1049).[39] Minor shifts in the (100) and (101) diffraction peaks towards lower angles were observed in the K-CdS samples, which may be associated with the incorporation of K^+ ions into the CdS lattice. This shift is attributable to local lattice expansion due to the larger ionic radius of K^+ (138 pm) compared to Cd^{2+} (97 pm).[40] X-ray photoelectron spectroscopy (XPS) analysis further confirmed the successful incorporation of K^+ into the CdS layer (Fig. 1b–d). Distinct K $2p_{3/2}$ and K $2p_{1/2}$ peaks are clearly observed, thus confirming the presence of K elements in the CdS film. Additionally, slight binding energy shifts in the Cd 3d and S 2p orbitals suggest that the local electronic environment is modified, likely due to an altered distribution of electron density in the Cd–S bonds.

This electronic restructuring may play a role in optimizing the energy level alignment and enhancing charge transfer across the heterojunction.[41] The surface morphologies of both CdS films are shown in Fig. S6. The KOH-treated CdS film exhibits a slightly more compact surface with a more uniform grain-size distribution. Atomic force microscope (AFM) analysis further reveals a slightly smoother and more homogeneous surface accompanied by a modest reduction in roughness, which is expected to mitigate interface-related defects and provide more favorable conditions for the subsequent growth of the Sb_2Se_3 layer. The UV-vis transmittance spectra (Fig. 1e) show that the KOH-treated CdS films also exhibit a significant increase in transmittance within the 300–550 nm wavelength range, effectively minimizing optical losses in the short-wavelength region, the corresponding optical bandgap characteristics are presented in Fig. S7. This improvement ensures that a greater photon flux reaches the absorber layer, thereby contributing to enhanced photogenerated carrier generation. The external quantum efficiency (EQE) spectra (Fig. 1f) further corroborate this optical enhancement, with the K-CdS device demonstrating a marked increase in short-wavelength EQE. This can be attributed to an improved utilization of incident photons in the ultraviolet and visible spectral ranges. Transient

absorption spectroscopy (TAS) was employed to probe the carrier dynamics within the CdS films. The TAS maps and delay time dependent TA spectra measured are shown in Fig. S8 and S9, providing the raw decay signals of the photoexcited carriers. Based on the normalized kinetic curves plotted in Fig. 1g, we extracted the lifetime components by fitting the decay, and the corresponding fitting parameters are summarized in Table S1. The resulting lifetime for the K-CdS sample is $\tau_1 = 1831.60$ ps, which is approximately 43% longer than that of the undoped CdS film ($\tau_2 = 1276.19$ ps). This suggests that the incorporation of K^+ effectively prolongs the carrier lifetime, which may be associated with the passivation of trap states within the CdS layer.[42] Based on the above characterizations, this K-doping approach not only enhances the optical transmittance of the CdS layer in the short-wavelength region but also improves the film's crystallinity and electrical properties. This provides a solid foundation for the subsequent fabrication of high-quality heterojunction interfaces and stable charge transport pathways.

In addition to the effective thinning of the CdS film and the regulation of its optoelectronic properties, further optimization of the orientation, structure, and optoelectronic performance of ultrathin Sb_2Se_3 films is crucial for the development of highly efficient semi-transparent Sb_2Se_3 thin-film solar cells. During the experimental process, we observed significant changes in the film's orientation, crystallinity, and optoelectronic properties as its thickness decreased. The device's efficiency declined significantly at lower thicknesses. Therefore, achieving a dynamic balance between thickness and efficiency is crucial in the development of semi-transparent thin-film solar cells.

To achieve the controlled fabrication of ultrathin Sb_2Se_3 films with superior crystallinity and optoelectronic performance, we employed a post-deposition magnetron sputtering-based Se compensation strategy. The corresponding schematic of the fabrication process is shown in Fig. S10, and in the following we refer to samples fabricated without the magnetron-sputtered Se layer as "W/O Se" and those with Se compensation as "W Se". We suspected that, without Se compensation, the Sb_2Se_3 absorber would exhibit disordered grain orientation and surface voids. These morphological deficiencies exacerbate interfacial defects and recombination centers, which significantly impede vertical carrier transport. In contrast, the introduction of high-energy Se species effectively passivates surface dangling bonds and fills structural voids while simultaneously promoting recrystallization and inducing a vertically-aligned grain orientation. The resulting film exhibits improved structural coherence and interface quality, which collectively facilitate efficient carrier separation and extraction and thereby enhance device performance. The schematic diagram is shown in Fig. 2a. The effectiveness of the magnetron-sputtered Se compensation process was further evaluated *via* SEM analysis under varying sputtering powers (Fig. 2b). At lower thicknesses, the Sb_2Se_3 film surface exhibited smaller grain sizes and higher void densities, which could lead to significant leakage currents within the device. At higher sputtering powers, the film exhibited larger and more densely packed grains, as

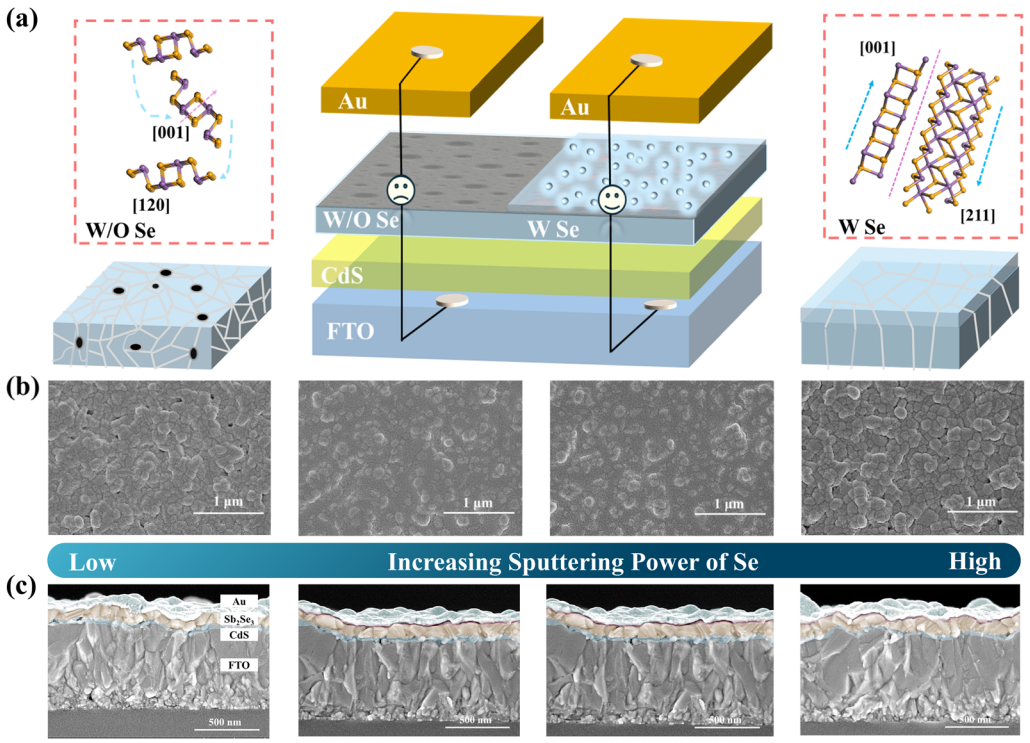

Fig. 2 (a) Schematic illustration of the Sb_2Se_3 device structure, comparing the layer configuration, crystal orientation, and vertical carrier transport pathways under conditions W/O Se and W Se compensation. (b) and (c) The surface and cross-sectional SEM images of Sb_2Se_3 films with Se interface layers deposited under different sputtering powers (0W, 18W, 22W, 26W).

well as reduced voids. This promotes the formation of continuous grains with preferentially oriented grain boundaries, suppressing carrier scattering and trap-assisted recombination and thus improving mobility and the efficiency of the charge transport pathways.[43] However, as the sputtering power increased beyond the optimal level, a decline in film crystallinity was observed, accompanied by the reappearance of surface voids. AFM analysis further corroborated the impact of varying Se sputtering powers on the surface morphology of Sb_2Se_3 films (Fig. S11). Under optimal sputtering conditions, the film exhibited the lowest root mean square roughness (R_q = 13.1 nm), which is indicative of a smooth and compact surface morphology. This observation is consistent with the uniform grain structure revealed by SEM, which further supports the conclusion that Se compensation facilitates grain densification and surface flattening. Contrastingly, deviating from the optimal sputtering power resulted in increased surface roughness and the formation of less compact morphologies. Cross-sectional SEM imaging (Fig. 2c) further confirms that the total thickness of the CdS/Sb_2Se_3/Se multilayer structure was precisely controlled within 80 nm—comprising 20 nm of CdS, 50 nm of Sb_2Se_3 absorber, and a 10 nm sputtered Se layer. Under optimized Se sputtering conditions, the Sb_2Se_3 grains exhibited a pronounced preferential orientation along the [*hk*1] crystallographic direction, forming vertically-aligned columnar structures across the entire thickness of the absorber layer. This vertical grain alignment, combined with an ultrathin architecture, suppresses recombination losses and provides a structurally favorable pathway for directional carrier transport.[44] This morphological ordering is critical for enhancing charge extraction and overall photovoltaic performance in ultrathin Sb_2Se_3-based devices.

Further crystallographic investigation was conducted to evaluate the influence of Se compensation on the crystal orientation and phase purity of Sb_2Se_3 thin films. As shown in Fig. 3a, XRD analysis reveals that the introduction of reactive Se *via* sputtering leads to a noticeable increase in the diffraction intensities of the [*hk*1] planes, particularly the (211) and (221) reflections.[45,46] This behavior suggests that Se compensation induces a certain degree of enhancement in [*hk*1]-oriented crystal growth. Quantitative analysis of the texture coefficient (TC) is consistent with this trend (Fig. S12): the (211) plane exhibits a TC value of 1.68 in the W Se sample, compared to 1.14 in its untreated counterpart.[22] These results indicate that Se incorporation moderately improves the degree of crystallographic orientation, which is expected to be beneficial for directional carrier transport and for mitigating recombination losses in ultrathin Sb_2Se_3 solar cells.[47,48]

To elucidate how post-selenization affects both the surface chemical states and the crystal structure, we performed a comprehensive analysis by combining XPS, depth-profiled XPS, and Raman spectroscopy. High-resolution Se 3d XPS spectra (Fig. 3b) reveal the coexistence of two distinct Se chemical states at the surface of the Se-treated Sb_2Se_3 film. The peaks located at 55.28 eV and 56.09 eV correspond to the Se $3d_{5/2}$ and $3d_{3/2}$ levels of elemental selenium (Se^0), signifying the formation of a metallic Se surface capping layer.[49] The peaks at 53.75 eV and 54.60 eV, on the other hand, are attributed to divalent selenium (Se^{2-}), suggesting the formation of Sb–Se bonds (through chemical interactions with Sb), which stabilize the surface bonding environment. The Sb 3d core-level spectra (Fig. 3c) reveal oxidation state variations between the W/O and W Se samples. Notably, the W Se film exhibits significantly reduced Sb–O signal and a sharper main Sb $3d_{5/2}$ peak at 529.39 eV with a smaller binding energy shift, indicating effective surface oxidation suppression. This is due to the compact Se^0 overlayer, which forms a physical barrier, thereby hindering oxygen adsorption and inhibiting subsequent Sb oxidation. To gain deeper insight into the vertical distribution of Se valence states, depth-resolved XPS analyses were conducted at etching depths of 0, 5, 15, and 20 nm (Fig. 3d). At the surface (0 nm), the Se^0 signal is predominant, indicating significant surface enrichment of elemental Se. As the etching depth increases, the Se^0 component progressively reduces while the Se^{2-} signal becomes increasingly prominent. This is due to the inward diffusion of Se atoms and the gradual formation of Sb–Se bonds induced by the post-selenization treatment.[50] Corresponding depth-profiled Sb 3d spectra (Fig. S13) reveal that the Sb–O species are restricted to the near-surface region, with negligible oxidation signatures detected within the bulk of the film. This vertically-graded distribution of Se^0 and Se^{2-} gives rise to a spatially modulated electronic structure which facilitates favorable interfacial band alignment, suppresses surface recombination *via* defect passivation, and effectively mitigates surface oxidation. Together, these synergistic effects provide a structurally and electronically optimized foundation for enhancing photovoltaic performance. Raman spectroscopy further confirms that Se treatment induces multiscale structural modulation. Under 532 nm excitation (Fig. 3e), both samples exhibit a prominent vibrational mode at 190 cm^{-1}, corresponding to the symmetric stretching of Sb–Se bonds.[51] This indicates that crystalline order is effectively preserved. Contrastingly, the defect-associated peak near 150 cm^{-1} (typically attributed to Sb–Sb bonds and structural disorder) is markedly suppressed following Se treatment, which indicates the successful mitigation of local Sb enrichment and its related defects. Additionally, weak signals are observed near 253 cm^{-1} and 295 cm^{-1}, likely corresponding to surface oxidation products such as Sb_2O_3. Under 785 nm excitation, the Se-treated sample maintains the characteristic Sb–Se vibrational peaks at 193 cm^{-1} and 209 cm^{-1}. An additional feature appears at 258 cm^{-1}. These can be attributed to Se–Se stretching modes of α-Se (Se_8 rings) or amorphous Se, indicating the formation of a Se-rich surface configuration during post-selenization. Notably, the weak peaks at 127 cm^{-1} and 158 cm^{-1} observed in the untreated film (commonly associated with Sb–Sb bonding or disordered domains) are completely absent following Se treatment. The quantitative analyses presented in Fig. 3f and g further support the above conclusions. As shown in Fig. 3f, the Se^0/Se^{2-} ratio gradually decreases with increasing etching depths. This indicates that Se^0 is mainly concentrated at the surface, whereas Se^{2-} becomes dominant in the deeper regions due to the progressive formation of Sb–Se bonds. This depth-dependent distribution confirms the inward diffusion of

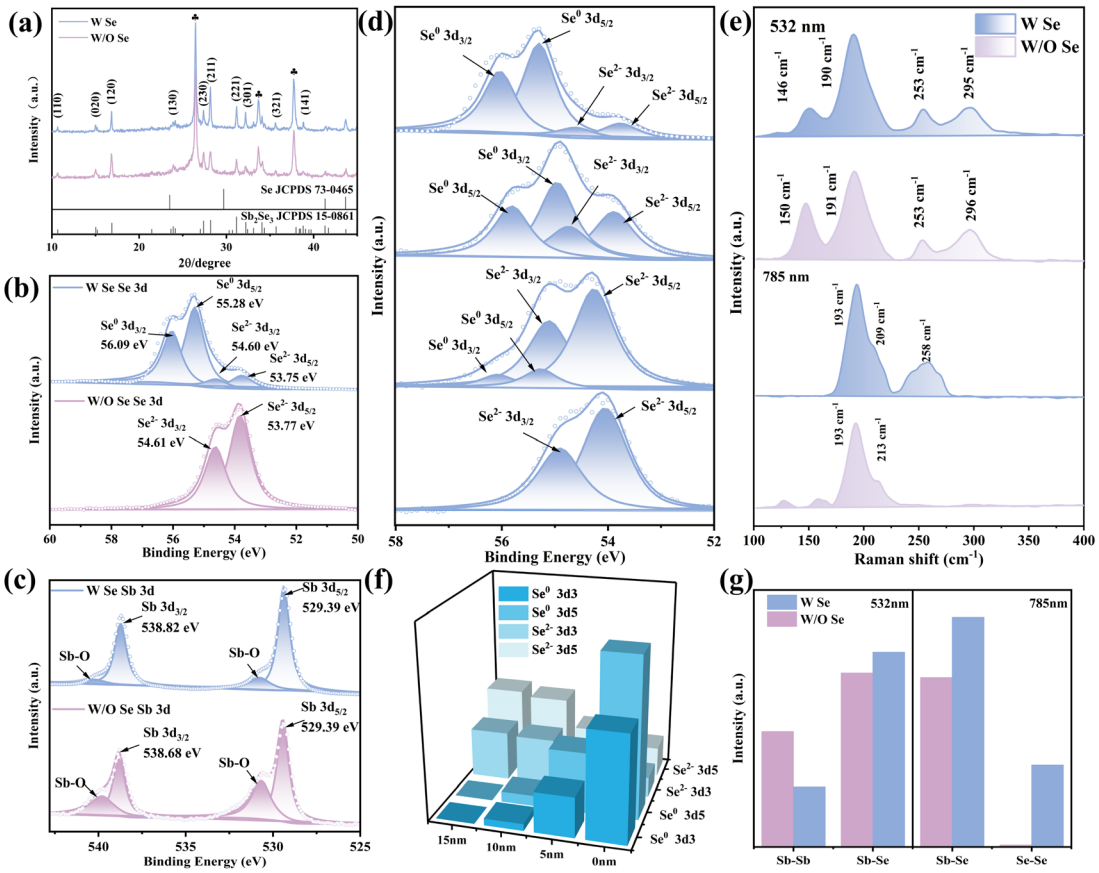

Fig. 3 (a) XRD patterns; (b) high-resolution XPS spectra of surface Se 3d; (c) high-resolution XPS spectra of Sb 3d; (d) depth-profiled XPS spectra of Se 3d; (e) Raman spectra excited at 532 nm and 785 nm; (f) Se^0/Se^{2-} ratio at different depths from XPS; (g) Raman intensity ratios of key bonds under two excitations.

Se during post-selenization. Meanwhile, the Raman intensity ratios in Fig. 3g reveal enhanced Sb–Se and Se–Se signals and a clear suppression of Sb–Sb modes in the Se-treated film. This corroborates the effective passivation of Sb_{Se} defects and the formation of a more ordered, Se-rich surface structure.

To gain deeper insight into the regulatory effect of Se compensation on the device's surface physical properties and energy band structure, Kelvin probe force microscopy (KPFM) was performed to comparatively characterize the W/O Se and W Se samples. Fig. S14 presents the corresponding KPFM surface morphology images of the W/O Se and W Se samples. As shown in Fig. 4a–d, the W/O Se samples exhibit pronounced fluctuations in surface potentials under both dark and illuminated conditions, along with a relatively higher average surface potential. This indicates severe Fermi-level pinning and a high density of surface trap states. On the other hand, the W Se sample displays a significantly lower and more uniform surface potential distribution, indicating a stabilized Fermi level and a reduced trap state density. The surface photovoltage (SPV) results obtained *via* KPFM (Fig. 4e and f) show that the SPV value of the W/O Se sample reached as high as 26.7 mV—considerably exceeding the 11.2 mV of the W Se sample. This difference reflects more pronounced surface charge accumulation under illumination in the W/O Se sample, stemming from abundant sub-bandgap trap states at the interface, which induce photogenerated carrier recombination. The reduced SPV values in the W Se sample indicate that Se compensation effectively passivates surface deep-level defects, suppresses interfacial non-radiative recombination, and prolongs carrier lifetime, thereby improving device performance.[52–54] Band alignment analysis (Fig. 4g and h) further elucidates the mechanism by which sputtered active Se modulates carrier transport and suppresses interfacial recombination. The ultraviolet photoelectron spectroscopy (UPS) spectra of the CdS buffer layer used for band alignment construction are shown in Fig. S15 and S16, and the corresponding UPS spectra and absorption characteristics of the Sb_2Se_3 films are provided in Fig. S17–S19. In the unoptimized C-Sb_2Se_3 interface, the conduction band minimum (CBM) of CdS appears significantly below that of Sb_2Se_3, resulting in a "cliff-like" band alignment with a conduction band offset (CBO) of approximately −0.11 eV.[42] This negative offset induces electron accumulation at the heterointerface and forces the photogenerated electrons to overcome an additional potential barrier, thereby intensifying Auger-type recombination driven by interfacial defect states. In contrast, the W Se interface optimized through Se sputtering exhibits significantly improved band alignment. The CBM of CdS (−3.73 eV) becomes slightly higher than that of

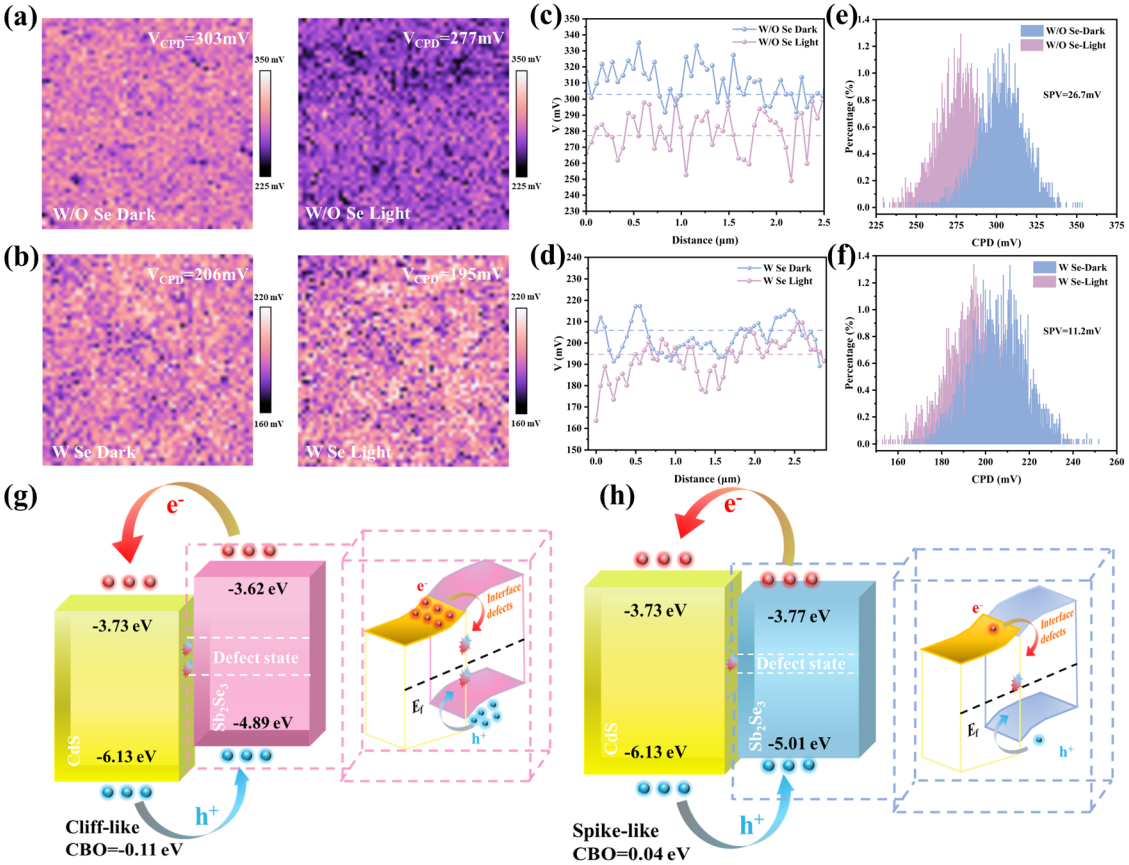

Fig. 4 (a and b) The KPFM (CPD) for the Sb_2Se_3 samples W/O and W Se; (c and d) corresponding surface potential line profiles; (e and f) statistical distribution histograms of surface potential for both samples; schematic energy band structures of the CdS/Sb_2Se_3 heterojunction W/O Se compensation (g) and W Se compensation (h).

Sb_2Se_3 (−3.77 eV), resulting in a "spike-like" conduction band offset of +0.04 eV.[55] This minor positive offset facilitates efficient electron tunneling *via* thermionic emission while simultaneously suppressing electron backflow at the interface. Compared to the cliff-like structure, the spike-like alignment provides a more favorable energy landscape for carrier transport, promoting the efficient extraction of photogenerated electrons and reducing interface-mediated recombination losses.

Any comprehensive evaluation of semitransparent photovoltaic devices critically depends on two key factors, namely, the intrinsic optical characteristics of the device (such as visible light transmittance and aesthetic appearance) and its PCE. Achieving an optimal balance between these parameters is essential for enabling practical applications—particularly in scenarios such as BIPV, where simultaneous energy generation and visual transparency are required. Fig. 5a provides a comparative visual representation of the optical appearance of three distinct Sb_2Se_3 films, namely, the unthinned 500 nm film, the ultrathin 50 nm W/O Se Sb_2Se_3 film, and the 50 nm W Se Sb_2Se_3 film treated with active Se. The 500 nm thick Sb_2Se_3 film exhibits a dark, opaque appearance, which is indicative of its strong light absorption and limited transmittance. In contrast, both the W/O Se Sb_2Se_3 and W Se Sb_2Se_3 films, upon being reduced to a thickness of 50 nm, exhibit markedly enhanced visible light transmittance and distinct semitransparent characteristics. Fig. 5b shows the *J–V* results for W/O Se and W Se Sb_2Se_3 solar cells, and Fig. S20 further compares the *J–V* curves of these ultrathin devices with those of the unthinned 500 nm Sb_2Se_3 solar cells. The detailed photovoltaic performance metrics of these devices are summarized in Table 1 and the corresponding *J–V* curves of devices with Se interface layers deposited at different sputtering powers are shown in Fig. S21. The results show that the short-circuit current density (J_{SC}) is significantly enhanced from 23.77 mA cm^{-2} for the W/O Se Sb_2Se_3 solar cells to 27.99 mA cm^{-2} after Se compensation, representing a notable 17.8% increase. This improvement is primarily attributed to enhanced light absorption and more efficient carrier collection. At the same time, the open-circuit voltage (V_{OC}) rises markedly from 0.219 V to 0.405 V, which is indicative of a substantial reduction in interfacial carrier recombination and improved built-in potential at the heterojunction interface. As a result, the PCE is dramatically improved from 1.82% to 7.02%, highlighting the pivotal role of Se compensation in modulating the optoelectronic properties and device energetics. In addition, light-intensity-dependent J_{SC} and V_{OC} characteristics (Fig. S22) further confirm the suppressed recombination in the Se-compensated devices. The statistical

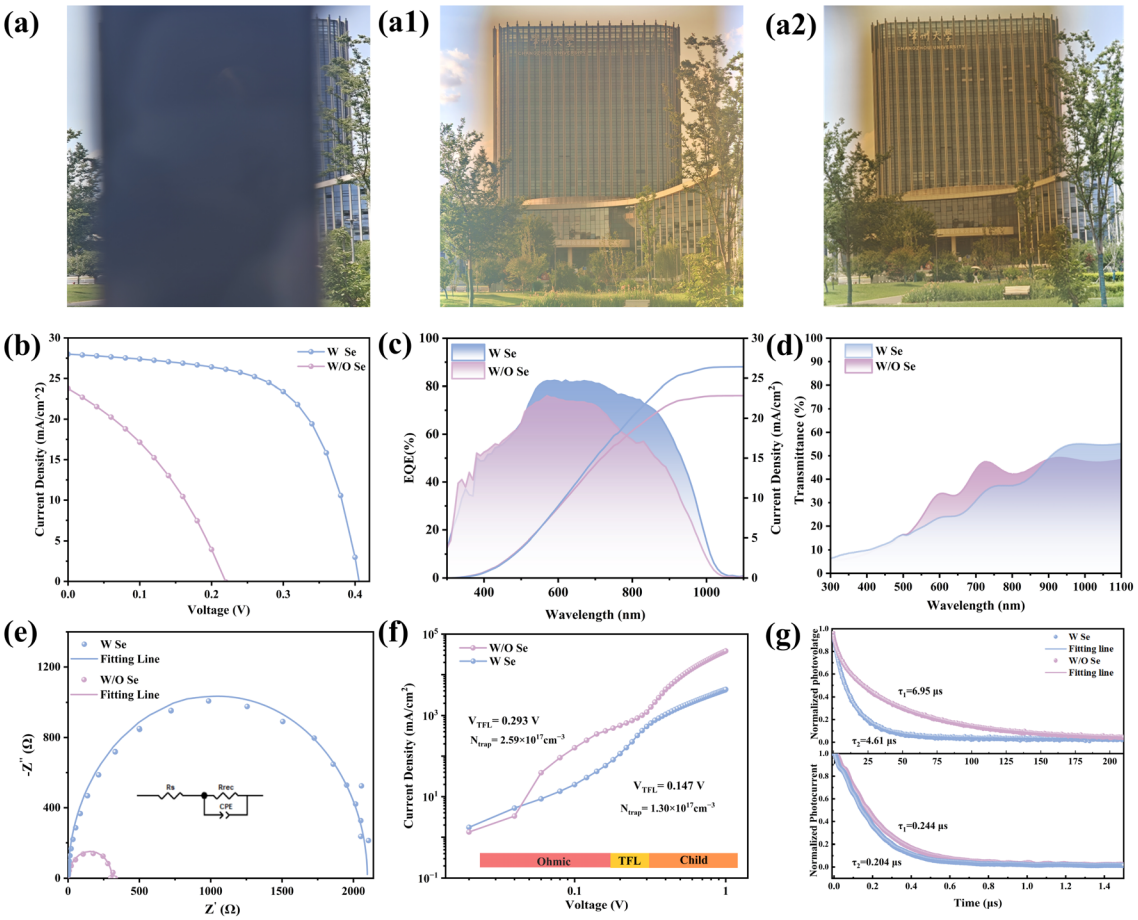

Fig. 5 Comparison of the semi-transparent appearance of (a) a 500 nm-thick Sb_2Se_3 film, (a1) an ultrathin 50 nm W/O Se film, and (a2) a W Se film treated with active Se. (b) *J*–*V* curves. (c) EQE plot, (d) transmission spectra, (e) Nyquist plots, (f) SCLC curves, (g) TPC and TPV decay curves of the corresponding Sb_2Se_3 solar cells.

Table 1 The detail photovoltaic parameters of correspond Sb_2Se_3 solar cells

Sample	V_{OC} (V)	J_{SC} (mA cm^{-2})	FF (%)	PCE (%)	R_S (Ω)	R_{sh} (Ω)
W/O Se	0.219	23.77	35.03	1.83	236	1927
W Se	0.405	27.99	61.82	7.02	117	8199

distribution of PCE values across multiple devices (Fig. S23) confirms the reliability and reproducibility of this performance enhancement, and a long-term stability test under ambient air (Fig. S24) demonstrates the enhanced stability of the W Se devices compared with the W/O Se references; both results together demonstrate the robustness of the post-selenization strategy. The EQE spectra and their corresponding integrated photocurrent densities are shown in Fig. 5c. The spectral response in the 600–1100 nm range is primarily attributable to the absorption characteristics of the Sb_2Se_3 absorber layer. Notably, the Se-compensated device exhibits a significantly enhanced photoresponse, particularly in the visible light wavelength region. This improvement is ascribed to the synergistic effects of the improved crystallinity, reduced bulk and interfacial recombination, and enhanced carrier transport properties induced by Se compensation.[56] Consequently, the integrated short-circuit current density derived from the EQE spectra increases from 22.84 mA cm^{-2} for the W/O Se device to 26.42 mA cm^{-2} for the W Se device, which further substantiates the role of Se incorporation in promoting efficient photogenerated carrier extraction and collection. The corresponding bandgap analysis based on these EQE spectra is summarized in Fig. S25, which is in good agreement with the bandgap values obtained from the absorption spectra. Upon thinning both the W/O Se and W Se Sb_2Se_3 films to 50 nm, the transmittance spectra (Fig. 5d) reveal that the W/O Se film exhibits enhanced optical transparency, with an average visible transmittance (AVT) of ≈25.82%, whereas the W Se film shows a moderately reduced AVT of ≈20.26% due to the additional Se incorporation. Despite this, both maintain significant visible-light transmittance, underscoring their potential for semi-transparent photovoltaic applications. These results underscore the feasibility of employing ultrathin Sb_2Se_3 absorbers in semitransparent photovoltaic applications. This is particularly relevant in BIPV, where a balance between light harvesting and transparency is essential. To further elucidate the effect of Se compensation on the carrier transport and recombination

dynamics, dark *J–V* measurements coupled with quantitative diode modeling were performed (Fig. S26a–d). A single-diode exponential model was employed to extract the key electrical parameters, including the reverse saturation current density (J_0), ideality factor (A), series resistance (R_S), and shunt conductance (G). These parameters collectively reflect the intrinsic diode quality and loss mechanisms. As illustrated in the differential conductance curve (dJ/dV *vs.*V, Fig. S26b), the G of the W/O Se device was measured at 15.399 mS cm^{-2}, whereas the W Se device exhibited a significantly reduced value of 0.126 mS cm^{-2}. This substantial reduction indicates the effective suppression of shunt leakage pathways.[57] In addition, the R_S and A, derived from the dJ/dV *vs.* $(J + J_{SC} - GV)^{-1}$ fitting (Fig. S26c), decreased from 2.23 Ω cm^2 and 1.66 in the W/O Se device to 1.72 Ω cm^2 and 1.55 in the W Se device, respectively. The lower A value reflects a reduction in trap-assisted recombination and an improvement in junction quality.[32] Furthermore, an analysis of the $\ln(J + J_{SC} - GV)$ *vs.* $(V - RJ)$ linear regime (Fig. S26d) reveals a marked decrease in the J_0, from 3.75×10^{-1} mA cm^{-2} in the control device to 1.30×10^{-3} mA cm^{-2} in the Se-compensated device. This two order of magnitude reduction in J_0 strongly suggests suppressed non-radiative recombination and reduced carrier leakage. These results collectively confirm that Se compensation not only improves the structural and interfacial properties of the Sb_2Se_3 absorber layer, but also significantly enhances charge transport and suppresses recombination losses, thereby contributing to the observed enhancement in V_{OC} and overall device performance.[58]

To further investigate the mechanisms underlying the performance enhancement induced by Se compensation, a series of transient electrical and carrier characterizations was conducted. The electrochemical impedance spectroscopy (EIS) results (Fig. 5e) were analysed using a simplified equivalent circuit consisting of a series resistance R_S and a parallel branch comprising the recombination resistance R_{rec} and a constant phase element (CPE). In this model, R_S represents the overall series resistance of the device, while R_{rec} corresponds to the recombination resistance associated with the CdS/Sb_2Se_3 junction region.[59] After Se treatment, the fitted R_{rec} increases whereas R_S decreases, a trend that is consistent with a reduced probability of nonradiative recombination in the junction region and lower resistive losses along the current path, that is, more efficient carrier transport in the device.[60] As shown in Fig. 5f, the space charge limited current (SCLC) measurements reveal a pronounced reduction in the trap-filled limit voltage (V_{TFL}) from 0.293 V to 0.147 V, corresponding to a decrease in trap density (N_{trap}) from 2.59×10^{17} cm^{-3} to 1.30×10^{17} cm^{-3}. This indicates the effective passivation of deep-level trap states within the bulk of the absorber layer. The capacitance–voltage ($C–V$) analysis provides further insights into the junction energetics. As shown in Fig. S27a, the built-in potential (V_{bi}) increased from 589 mV to 636 mV following active Se compensation. Meanwhile, the depletion width (W_d) expanded from 96.56 nm to 128.70 nm (Fig. S27b). These changes strengthen the internal electric field and enhance the spatial separation of photogenerated carriers, both of which contribute to improved charge collection. Transient photocurrent (TPC) analysis (Fig. 5g) shows that the electron transit time (τ_2) slightly increased as a result of Se treatment, which is indicative of efficient carrier extraction and interfacial transport. Meanwhile, the transient photovoltage (TPV) measurements reveal a prolonged dominant carrier lifetime (τ_1), increasing from 4.61 μs to 6.95 μs. The detailed fitting parameters used in the TPC and TPV analyses are summarized in Tables S2 and S3. This further confirms the suppression of nonradiative recombination pathways due to effective defect passivation.

Deep-level transient spectroscopy (DLTS) analysis further verifies the critical role of Se in defect regulation. As shown in Fig. 6a–c, two distinct deep-level defects were identified in the untreated semi-transparent Sb_2Se_3 films, namely, an electron trap (E1) with an activation energy of 0.662 eV and a hole trap (H1) with an activation energy of 0.742 eV. Based on capture cross-section analysis and earlier reports in the literature, E1 is attributed to V_{Se}, while H1 originates from Sb_{Se}.[60–62] As listed in Table 2, the concentration of the H1 trap in the W/O Se sample (4.02×10^{15} cm^{-3}) is significantly higher than that of E1 (5.57×10^{14} cm^{-3}), which further confirms the substantial presence of Sb_{Se} defects in the untreated film. During the preparation of semi-transparent Sb_2Se_3 films *via* RTE, the high evaporation rate and locally insufficient Se pressure readily induce Se-deficient regions, thereby synergistically promoting the formation of both V_{Se} and Sb_{Se} defects.[29] In the subsequent magnetron sputtering process that introduces reactive Se for compensation, the Se-rich environment facilitates Se atom diffusion into the film, effectively filling V_{Se} and suppressing the formation of Sb_{Se} defects.[63,64] Consequently, the H1 defect was completely passivated after Se treatment. The concentration of E1 was markedly reduced from 5.57×10^{14} cm^{-3} to 3.82×10^{14} cm^{-3}, with its capture cross-section σ decreasing from 2.79×10^{-14} cm^2 to 1.94×10^{-15} cm^2. These results clearly demonstrate the effective regulation of deep-level defects in Sb_2Se_3 films following reactive Se compensation. The energy band diagrams (Fig. 6d and e) further provide an intuitive depiction of the interfacial energy level changes induced by defect passivation. In the untreated sample, the defect levels E1 and H1 (located near the Fermi level) readily serve as nonradiative recombination centers and thereby cause significant photovoltaic losses. In contrast, after Se compensation, the band structure of the W Se film is more well-defined, with defect states positioned further away from E_f. This leads to a notable suppression of the nonradiative recombination of interfacial carriers. TAS measurements (Fig. 6f) further confirm the improved carrier dynamics. The corresponding TAS mapping results of the W and W/O Se Sb_2Se_3 films are presented in Fig. S28. Under excitation with a 400 nm pulsed laser, the decay curve reveals that the carrier lifetime τ_2 increased significantly from 53.8 ps to 122.8 ps following Se treatment, and the corresponding fitting parameters are listed in Table S4. This increase in lifetime is highly consistent with the reduced defect density observed in the DLTS measurements, confirming that Se compensation effectively mitigates carrier recombination associated with deep-level defects, thereby enhancing carrier extraction and transport.[65]

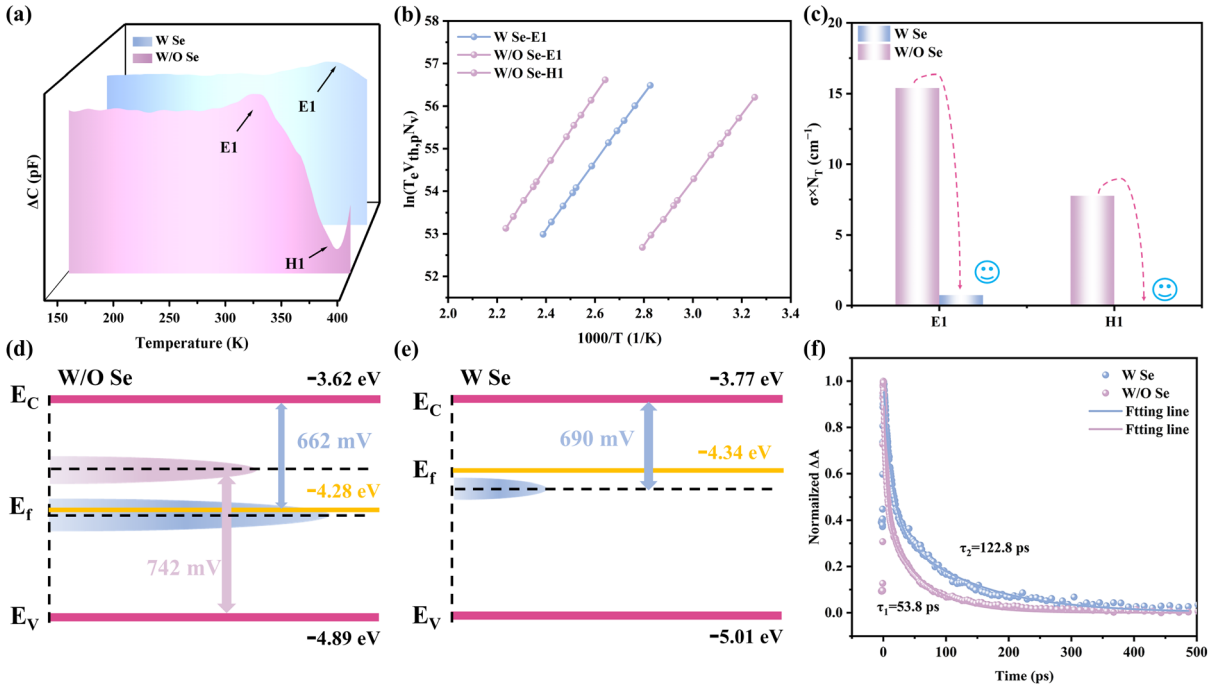

Fig. 6 (a) The capacitance variation of W/O Se and W Se samples at different temperatures. (b) Arrhenius plots; (c) comparison of $\sigma \times N_t$ values; (d and e) defect energy level diagrams of the Sb_2Se_3 solar cells with and without Se; (f) carrier lifetime of the Sb_2Se_3 solar cells with and without Se.

Table 2 The detail DLTS parameters of Sb_2Se_3 solar cell with and without Se

Sample	Defects	E_T (eV)	N_T (cm^{-3})	σ (cm^2)	$N_T \times \sigma$ (cm^{-1})	τ (s)
W/O Se	E1	0.662	5.57×10^{14}	2.79×10^{-14}	15.54	6.43×10^{-9}
	H1	0.742	4.02×10^{15}	1.93×10^{-15}	7.76	1.29×10^{-8}
W Se	E1	0.690	3.82×10^{14}	1.94×10^{-15}	0.74	1.35×10^{-7}

Collectively, these results demonstrate that Se compensation synergistically enhances device performance by simultaneously reducing deep-level defect density, strengthening the built-in electric field, and facilitating more efficient carrier transport and extraction. These improvements provide a solid physical basis for the significant gains in V_{OC}, J_{SC}, and overall efficiency observed in ultrathin semi-transparent Sb_2Se_3 solar cells following Se compensation.

Experimental section

The experimental details are given in the SI.

Conclusion

In this study, a synergistic strategy combining functional thinning and defect regulation was employed to systematically enhance the optoelectronic performance of ultrathin semi-transparent Sb_2Se_3 solar cells. Initially, KOH doping was utilized to thin the CdS buffer layer, which not only improved the short-wavelength transmittance of the device but also optimized the heterojunction interface quality, thereby establishing a favorable foundation for subsequent Se compensation. Reactive Se was then introduced *via* magnetron sputtering to compensate the ultrathin Sb_2Se_3 absorber layer prepared *via* RTE. Comprehensive characterizations reveal that this approach significantly improved the crystallographic orientation and structural integrity of the films, with a notable enhancement in [*hk*1] preferential orientation. A combination of advanced techniques further elucidated the critical role of Se compensation in modulating interfacial band alignment, suppressing Fermi-level pinning, and passivating deep-level defects. Notably, non-radiative recombination centers such as V_{Se} and Sb_{Se} were effectively mitigated, leading to prolonged carrier lifetimes and reduced recombination losses. As a result, the device efficiency was markedly improved from 1.82% to 7.02% while maintaining high visible light transmittance. This work provides essential theoretical insights and technical guidance for the efficient design and practical application of semi-transparent Sb_2Se_3 thin-film solar cells.

Author contributions

Huafei Guo conceived the idea, designed the experiments, provided funding support, and revised the manuscript. Bangzhi Shen assisted with experimental design and implementation,

and wrote the initial draft. Xing Wang, Jiayu Xiao carried out experimental operations and contributed to data analysis. Wenyun Deng, Sai Jiang, Lei Xu, Xu-Dong, and Lvzhou Li participated in experimental implementation. Shuai Zhang and Jianhua Qiu contributed to manuscript revision. Ningyi Yuan and Jianning Ding also provided financial support and revised the manuscript. All authors discussed the results and commented on the manuscript. Huafei Guo, Xu-Dong, and Jianhua Qiu are the corresponding authors.

Conflicts of interest

There are no conflicts to declare.

Data availability

The data that support the findings of this study are available from the corresponding author upon reasonable request.

Supplementary information (SI): detailed experimental and device fabrication procedures, calculation and fitting methods, additional tables, and extensive characterization data (XRD, SEM, AFM, TAS, TPV, TPC, *C–V*, SCLC, DLTS, XPS, UPS, EQE, and *J–V*) supporting the conclusions of this work. See DOI: https://doi.org/10.1039/d5sc08223d.

Acknowledgements

This work was also supported by Changzhou University, National Science Foundation of China (Grant No. 62504024, 62505032, 62206030), China Postdoctoral Science Foundation (Certificate Number: 2025M770524), Natural Science Foundation of Jiangsu Province (Grant No. BK20220624), Changzhou Sci & Tech Program (Grant No. CJ20241086), Natural Science Foundation of Yangzhou (YZ2024177), Yangzhou Innovation Capability Enhancement Program (YZ2022170).

Notes and references

1 P. Kumar, S. You and A. Vomiero, *Adv. Energy Mater.*, 2023, **13**, 2301555.
2 Y. Zhou, C. Xiang, Q. Dai, S. Xiang, R. Li, Y. Gong, Q. Zhu, W. Yan, W. Huang and H. Xin, *Adv. Energy Mater.*, 2023, **13**, 2300253.
3 D. Girolamo, G. Vidon, J. Barichello, F. Giacomo, F. Jafarzadeh, B. Paci, A. Generosi, M. Kim, L. Castriotta, M. Frégnaux, J. Guillemoles, F. Brunetti, P. Schulz, D. Ory, S. Cacovich, A. Carlo and F. Matteocci, *Adv. Energy Mater.*, 2024, **14**, 2400663.
4 Y. Zhang, H. Xia, J. Yu, Y. Yang and G. Li, *Adv. Mater.*, 2025, 2504063.
5 C. Chen, L. Wang, W. Xia, K. Qiu, C. Guo, Z. Gan, J. Zhou, Y. Sun, D. Liu, W. Li and T. Wang, *Nat. Commun.*, 2024, **15**, 6865.
6 V. Wong, J. Ho, W. Wong and S. So, *Energy Environ. Sci.*, 2025, **18**, 579–601.
7 M. Shin, A. Lee, A. Cho, K. Kim, S. Ahn, J. Park, J. Yoo, J. Yun, J. Gwak, D. Shin, I. Jeong and J. Cho, *Nano Energy*, 2021, **82**, 105729.
8 X. Yang, J. Han, W. Ruan, Y. Hu, Z. He, X. Jia, S. Zhang and D. Wang, *Chin. Chem. Lett.*, 2022, **33**, 1425–1429.
9 Z. Wei, B. Smith, F. Rossi, J. Searle, D. Worsley and T. Watson, *J. Mater. Chem. C*, 2019, **7**, 10981–10987.
10 T. Li, M. Almutairi, J. Ma, A. Stewart, Z. Xing, M. Liu, B. Hou and Y. Cho, *Nano-Micro Lett.*, 2025, **17**, 49.
11 Z. Li, X. Liang, G. Li, H. Liu, H. Zhang, J. Guo, J. Chen, K. Shen, X. San, W. Yu, R. Schropp and Y. Mai, *Nat. Commun.*, 2019, **10**, 120.
12 X. Wang, S. Kavanagh, D. Scanlon and A. Walsh, *Joule*, 2024, **8**, 2105.
13 Q. Zhao, B. Che, H. Wang, X. Peng, J. Yang, R. Tang, C. Zhu and T. Chen, *J. Mater. Chem. A*, 2024, **12**, 11524–11534.
14 Q. Zhao, R. Tang, B. Che, Y. He, T. Wu, X. Peng, J. Yang, S. Sheng, C. Zhu and T. Chen, *Adv. Mater.*, 2025, **37**, 2414082.
15 C. Qian, K. Sun, J. Cong, H. Cai, J. Huang, C. Li, R. Cao, Z. Liu, M. Green, B. Hoex, T. Chen and X. Hao, *Adv. Mater.*, 2023, **35**, 2303936.
16 Y. Zhao, S. Wang, C. Li, B. Che, X. Chen, H. Chen, R. Tang, X. Wang, G. Chen, J. Gong, T. Chen, X. Xiao and J. Li, *Energy Environ. Sci.*, 2022, **15**, 5118.
17 R. Tang, X. Chen, G. Liang, Z. Su, J. Luo and P. Fan, *Surf. Coat. Technol.*, 2019, **360**, 68–72.
18 R. Tang, Z. Zheng, Z. Su, X. Li, Y. Wei, X. Zhang, Y. Fu, J. Luo, P. Fan and G. Liang, *Nano Energy*, 2019, **64**, 103929.
19 Y. Luo, R. Tang, S. Chen, J. Hu, Y. Liu, Y. Li, X. Liu, Z. Zheng, Z. Su, X. Ma, P. Fan, X. Zhang, H. Ma, Z. Chen and G. Liang, *Chem. Eng. J.*, 2020, **393**, 124599.
20 R. Jakomin, S. Rampino, G. Spaggiari and F. Pattini, *Solar*, 2023, **3**, 566–595.
21 P. Kumar, P. Kumar, J. Thomas, A. Gradone, N. Gilli, S. You, V. Morandi, K. Leung and A. Vomiero, *Adv. Sci.*, 2025, e12103.
22 H. Guo, S. Huang, H. Zhu, T. Zhang, K. Geng, S. Jiang, D. Gu, J. Su, X. Lu, H. Zhang, S. Zhang, J. Qiu, N. Yuan and J. Ding, *Adv. Sci.*, 2023, **10**, 2304246.
23 X. Liu, Y. Liu, S. Zhang, X. Sun, Y. Zhuang, J. Liu, G. Wang, K. Cheng and Z. Du, *Small Methods*, 2024, **8**, 2300728.
24 G. Liang, M. Chen, M. Ishaq, X. Li, R. Tang, Z. Zheng, Z. Su, P. Fan, X. Zhang and S. Chen, *Adv. Sci.*, 2022, **9**, 2105142.
25 K. Peng, Z. Wu, X. Liu, J. Yang and Z. Guan, *Small*, 2025, **21**, 2406035.
26 H. He, Y. Zhong, W. Zou, X. Zhang, J. Zhao, M. Ishaq and G. Liang, *Surf. Interfaces*, 2024, **51**, 104793.
27 S. Yuan, H. Deng, X. Yang, C. Hu, J. Khan, W. Ye, J. Tang and H. Song, *ACS Photonics*, 2017, **4**, 2862–2870.
28 Z. Cai, B. Che, Y. Gu, P. Xiao, L. Wu, W. Liang, C. Zhu and T. Chen, *Adv. Mater.*, 2024, **36**, 2404826.
29 V. Kumar, E. Artegiani, P. Punathil, M. Bertoncello, M. Meneghini, F. Piccinelli and A. Romeo, *ACS Appl. Energy Mater.*, 2021, **4**, 12479–12486.
30 Z. Chen, X. Guo, H. Guo, C. Ma, J. Qiu, N. Yuan and J. Ding, *Mater. Lett.*, 2019, **236**, 503–505.

31 K. Shen, Y. Zhang, X. Wang, C. Ou, F. Guo, H. Zhu, C. Liu, Y. Gao, R. Schropp, Z. Li, X. Liu and Y. Mai, *Adv. Sci.*, 2020, **7**, 2001013.
32 X. Wen, Z. Lu, X. Yang, C. Chen, M. Washington, G. Wang, J. Tang, Q. Zhao and T. Lu, *ACS Appl. Mater. Interfaces*, 2023, **15**, 22251–22262.
33 A. Hajjiaha and N. Gorji, *Sol. Energy Mater. Sol. Cells*, 2024, **270**, 112828.
34 K. M. Mamta and V. Singh, *Sustainability*, 2021, **13**, 12320.
35 J. Mendes, E. Gaspera and J. Embden, *Sol. RRL*, 2022, **6**, 2200265.
36 L. Guo, C. Grice, B. Zhang, S. Xing, L. Li, X. Qian and F. Yan, *Sol. Energy*, 2019, **188**, 586–592.
37 K. Cho, J. Jang, J. Park, D. Lee, S. Song, K. Kim, Y. Eo, J. Yun, J. Gwak and C. Chung, *ACS Omega*, 2020, **5**, 23983–23988.
38 D. Qin, P. Yang, Y. Pan, Y. Wang, Y. Pan, G. Weng, X. Hu, J. Tao, J. Chu, H. Akiyama and S. Chen, *ACS Appl. Mater. Interfaces*, 2025, **17**, 22050–22059.
39 Z. Cao, B. Shao, Z. Ye, C. Liu, Z. Li, J. Dong, W. Wang, J. Li, H. Liu and Y. Zhang, *Adv. Funct. Mater.*, 2025, **35**, 2418974.
40 H. Ning, H. Guo, J. Zhang, X. Wang, X. Jia, J. Qiu, N. Yuan and J. Ding, *Sol. Energy Mater. Sol. Cells*, 2021, **221**, 110816.
41 A. Mo, B. Yang, X. Lu, Y. Duan, X. Liang, Z. Zhang, Y. Guo and Z. Li, *Adv. Funct. Mater.*, 2025, **35**, 2420261.
42 T. Zhang, Y. Yang, J. Dong, B. Shen, J. Zhang, S. Zhang, H. Zhang, M. Lu, S. Jiang, J. Qiu, L. Li, H. Zhuang, H. Guo, N. Yuan and J. Ding, *Adv. Funct. Mater.*, 2025, **35**, 2417868.
43 Z. Duan, X. Liang, Y. Feng, H. Ma, B. Liang, Y. Wang, S. Luo, S. Wang, R. Schropp, Y. Mai and Z. Li, *Adv. Mater.*, 2022, **34**, 2202969.
44 A. Mo, Y. Feng, B. Yang, W. Dang, X. Liang, W. Cao, Y. Guo, T. Chen and Z. Li, *Adv. Funct. Mater.*, 2024, **34**, 2316292.
45 Y. Mo, C. Li, J. Yang, X. Wang, P. Hu, X. Chen, T. Chen, X. Xiao and J. Li, *Adv. Mater.*, 2025, **37**, e06372.
46 Y. Lin, C. Chang and Y. Hung, *Sol. Energy Mater. Sol. Cells*, 2019, **64**, 103929.
47 Y. Zhou, L. Wang, S. Chen, S. Qin, X. Liu, J. Chen, D. Xue, M. Luo, Y. Cao, Y. Cheng, E. Sargent and J. Tang, *Nat. Photonics*, 2015, **9**, 409–415.
48 K. Li, R. Tang, C. Zhu and T. Chen, *Adv. Sci.*, 2024, **11**, 2304963.
49 B. Canavaa, J. Vignerona, A. Etcheberrya, J. Guillemolesb and D. Lincot, *Appl. Surf. Sci.*, 2002, **202**, 8–14.
50 I. Caño, P. Fuentes, L. Barrio, X. Alcobé, J. Asensi, S. Giraldo, Y. Sánchez, Z. Jehl, M. Placidi, J. Puigdollers, V. Roca and E. Saucedo, *ACS Appl. Mater. Interfaces*, 2022, **14**, 11222–11234.
51 A. Kumar, V. Kumar, A. Romeo, C. Wiemer and G. Mariotto, *J. Phys. Chem. C*, 2021, **125**, 19858–19865.
52 S. Rijal, D. Li, R. Awni, C. Xiao, S. Bista, M. Jamarkattel, M. Heben, C. Jiang, M. Jassim, Z. Song and Y. Yan, *Adv. Funct. Mater.*, 2022, **32**, 2110032.
53 X. Wen, Z. Lu, G. Wang, M. Washington and T. Lu, *Nano Energy*, 2021, **85**, 106019.
54 X. Liang, Y. Feng, W. Dang, H. Huang, X. Wang, Y. Guo, K. Shen, R. Schropp, Z. Li, Y. Mai and A. C. S. Energy, *Lett*, 2023, **8**, 213.
55 Y. Luo, G. Chen, S. Chen, N. Ahmad, M. Azam, Z. Zheng, Z. Su, M. Cathelinaud, H. Ma, Z. Chen, P. Fan, X. Zhang and G. Liang, *Adv. Funct. Mater.*, 2023, **33**, 2213941.
56 C. Zhang, R. Jiang, Y. Zheng, Y. Li, Z. Cai, C. Ma, Y. Cheng, J. Chu and J. Tao, *Adv. Energy Mater.*, 2025, **15**, 2403352.
57 X. Wang, R. Tang, C. Jiang, W. Lian, H. Ju, G. Jiang, Z. Li, C. Zhu and T. Chen, *Adv. Energy Mater.*, 2020, **10**, 2002341.
58 G. Liang, Y. Luo, S. Chen, R. Tang, Z. Zheng, X. Li, X. Liu, Y. Liu, Y. Li, X. Chen, Z. Su, X. Zhang, H. Ma and P. Fan, *Nano Energy*, 2020, **73**, 104806.
59 S. Vijayaraghavan, K. Khawaja, J. Wall, W. Xiang and F. Yan, *Energy Adv.*, 2024, **3**, 1054–1061.
60 W. Lian, R. Cao, G. Li, H. Cai, Z. Cai, R. Tang, C. Zhu, S. Yang and T. Chen, *Adv. Sci.*, 2022, **9**, 2105268.
61 X. Wen, C. Chen, S. Lu, K. Li, R. Kondrotas, Y. Zhao, W. Chen, L. Gao, C. Wang, J. Zhang, G. Niu and J. Tang, *Nat. Commun.*, 2018, **9**, 2179.
62 B. Che, Z. Cai, H. Xu, S. Sheng, Q. Zhao, P. Xiao, J. Yang, C. Zhu, X. Zheng, R. Tang and T. Chen, *Angew. Chem.*, 2025, **137**, e20242563.
63 X. Liu, X. Xiao, Y. Yang, D. Xue, D. Li, C. Chen, S. Lu, L. Gao, Y. He, M. Beard, G. Wang, S. Chen and J. Tang, *Prog. Photovolt: Res. Appl*, 2017, **25**, 861–870.
64 J. Kim, S. Ji, Y. Jang, G. Jeong, J. Choi, D. Kim, S. Nam and B. Shin, *Sol. RRL*, 2021, **5**, 2100327.
65 B. Shen, T. Zhang, J. Dong, J. Zhang, B. Dong, H. Zhang, S. Jiang, D. Gu, L. Li, S. Zhang, J. Qiu, H. Guo, N. Yuan and J. Ding, *Adv. Funct. Mater.*, 2025, **35**, 2503922.